Creating Isolated Liquid Compartments Using Photopatterned Obstacles in Microfluidics

Hyundo Lee, Ankur Gupta, T. Alan Hatton, and Patrick S. Doyle*
Massachusetts Institute of Technology, Cambridge, Massachusetts 02139, USA
(Received 5 December 2016; revised manuscript received 24 February 2017; published 19 April 2017)

We propose a method to trap liquid (both oil and water) in a microchannel by sequentially injecting oil and water (or vice versa) over photopatterned obstacles with controlled wetting properties. We present a simple geometrical model to understand the liquid-entrapment process and predict the evolution of the water/oil interface over an obstacle. Our analysis provides an analytic solution that can successfully predict useful properties such as angular position of pinch-off and the amount of captured liquid. We show that we are able to obtain a liquid bridge over two circular obstacles, and we are also able to predict the condition for the formation of a bridge. We further demonstrate the effect of the obstacle shape and how a sudden change in gradient results in larger liquid entrapment. We also demonstrate the ability to entrap isolated liquid chambers for parallel experimentation.

DOI: 10.1103/PhysRevApplied.7.044013

I. INTRODUCTION

A method to create liquid chambers at small length scales can enable a large number of parallel experiments to be conducted in a small device. For instance, isolated nanoliter water pockets in a microchannel, much like a multiwell plate system, can be used for applications in diagnostics, drug discovery, and hydrogel synthesis [1–5]. Similarly, entrapped oil pockets can be used to study reaction engineering and to screen chemicals for enhanced oil recovery [6]. In the literature, there are two broad categories of studies related to liquid entrapment. The first focuses on the design of microfabricated traps such as depressions and other lithographic features for entrapment of individual droplets [7–15]. In contrast, the second focuses on the design of a complex porous network for larger-scale liquid entrapment [16–26]. Though the studies in the first category are able to trap individual droplets, they typically cannot control the shape of trapped droplets. The second category of studies can produce designed or random morphologies of liquid entrapment, but they are unable to trap isolated well-defined liquid pockets.

In this article, we present a method to trap isolated liquid regions in a fluidic device. This is achieved by sequentially flowing oil and water (or vice versa) past photopatterned obstacles with tailored wetting properties [27]. The simplicity of the proposed method allows us to control the amount and shape of entrapped liquid by using size, shape, and wettability of the obstacles as design parameters. Our method allows us to trap oil as well as water pockets. Further, we also detail the underlying mechanism of liquid entrapment through a simple model that has an analytical solution. The model is able to give insights into the importance of wetting and geometry in controlling the entrapment process that can have broad implications in multiphase flows.

*pdoyle@mit.edu

II. RESULTS AND DISCUSSION

A. One circular post: Theory and experiments

1. Experimental setup

A schematic of our experimental setup to trap oil is presented in Fig. 1(a). Following a process previously developed by our group [27], we photopattern a post with controlled wetting properties within a glass microchannel with height 50 μm, width 1 mm, and length 18 mm (Hilgenberg GmbH). We tailor the wetting properties of the post by varying the ratio of the monomer and cross-linker in the photopolymer mixture. By using different proportions of lauryl acrylate (monomer, Sigma-Aldrich) and 1,6-hexanediol diacrylate (cross-linker, Sigma-Aldrich), we create posts with five different wetting properties (details of the photopolymer composition and contact-angle measurements are provided in the Appendix). For the most oil-wet case, the post has $\theta_{a,\mathrm{WO}} = 144°$ (the advancing contact angle of water in oil) and $\theta_{r,\mathrm{WO}} = 111°$ (the receding contact angle of water in oil). On the other hand, for the least oil-wet case, the post has $\theta_{a,\mathrm{WO}} = 95°$ and $\theta_{r,\mathrm{WO}} = 82°$.

After photopattering the post, the channel is sequentially filled with decane (Sigma-Aldrich) and water by a syringe pump (Harvard Apparatus) at a constant flow rate of 9 μL/ min. The encapsulation of oil behind the obstacle involves (1) a decrease in the interfacial curvature when water reaches the obstacle, (2) oleophilic wetting leading to bending of the interface as it moves over the obstacle, and (3) pinch-off when two sides of the interface meet each other [Fig. 1(b)].

The procedure to trap water is the same except that it involves creating a water-wet post and sequentially

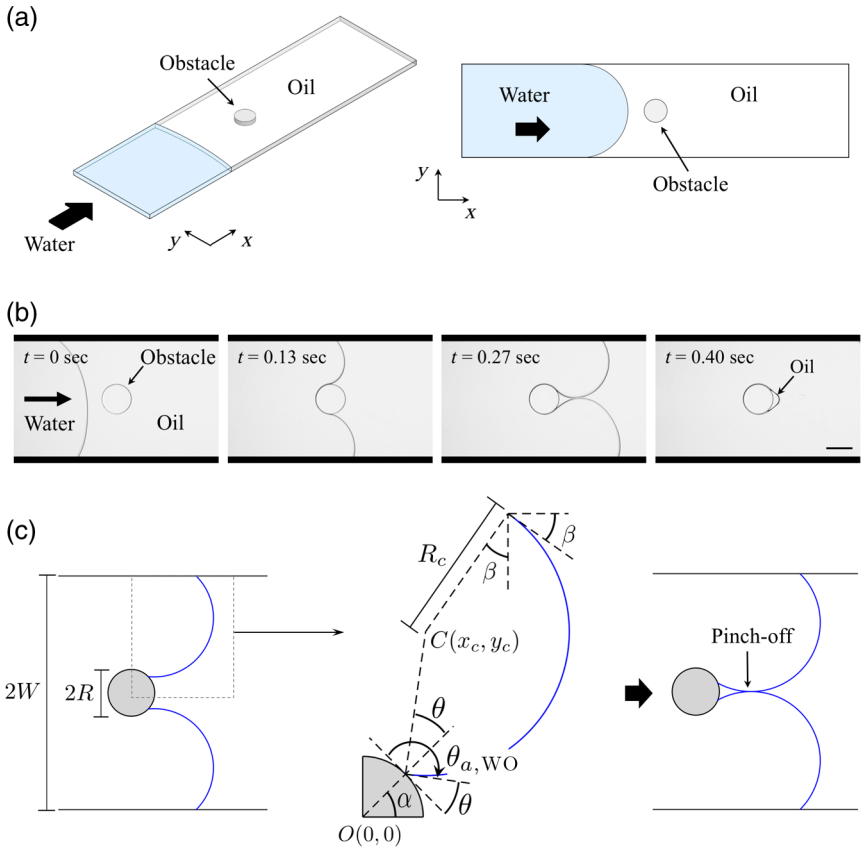

FIG. 1. Schematics of the experimental and theoretical setup. (a) Schematic of immiscible liquid-liquid displacement in a microchannel with an obstacle. For oil entrapment, an oil-wet circular post is first patterned in a flat glass microchannel, the channel is filled with decane (oil), and water is introduced into the channel. For water entrapment, we create a water-wet post and sequentially flow water and decane (oil). (b) Time-series microscope images through the immiscible displacement process for oil entrapment. As displacing water meets the obstacle, the water/oil interface starts to bend and encapsulates the obstacle, and the interface pinches off when the upper and lower interfaces touch each other at the center line of the channel. As a result, an oil pocket is left at the posterior region of the obstacle. Scale bar is 200 μm. (c) Schematic of theoretical setup. Because of the low capillary number of the outer water flow $O(10^{-5})$, the water/oil interface can be approximated as a circular arc with boundary conditions specified by the contact angles with the two solid surfaces—the obstacle and the channel sidewall.

injecting water and decane (i.e., the inverse of the oil case). We photopattern a water-wet post with $\theta_{a,\mathrm{WO}} = 67°$, $\theta_{r,\mathrm{WO}} = 40°$ using a specific composition of hydrophilic monomer additive 2-hydroxyethyl acrylate (Sigma-Aldrich) and hydrophilic cross-linker 1-(acryloyloxy)-3-(methacryloyloxy)-2-propanol (Sigma-Aldrich). Details of the compositions and contact angles are provided in the Appendix.

2. Theoretical setup

There are several important dimensionless numbers for the given system: the Reynolds number $\mathrm{Re} = (\rho_w u_{\mathrm{av}} H/\mu_w)$, viscosity ratio (μ_o/μ_w), capillary number $\mathrm{Ca} = (\mu_w u_{\mathrm{av}}/\sigma)$, contact angle of oil in water on the post θ, contact angle of oil in water with the sidewalls β, and geometric ratio R/W, where ρ_w is the density of the water, u_{av} is the gap-average velocity of water, μ_w is the viscosity of the water, H is the half-height of the channel, μ_o is the viscosity of decane, σ is the interfacial tension between water and decane, R is the radius of the post, and W is the half-width of the channel.

We can obtain important insights into the system by estimating the values of some of the dimensionless numbers. By using the physical properties of water and $u_{\mathrm{av}} \approx 3$ mm/s (calculated by dividing the injection flow rate by the cross-sectional area), we calculate $\mathrm{Re} \sim O(10^{-1})$. This low Reynolds number implies that the flow around the post is laminar and symmetric. μ_o/μ_w for decane and water is close to unity, and, thus, we can neglect any viscosity contrast effects. Lastly, by assuming $\sigma \approx 50 \times 10^{-3}$ N/m, we estimate $\mathrm{Ca} \sim O(10^{-4})$. Low values of Ca signify that the interface between oil and water is not perturbed by the shear forces and that we can use a pseudostatic assumption for the interface at each instant in time. Upon varying the input flow rate by 3 orders of magnitude (0.1 mm/s $\leq u_{\mathrm{av}} \leq$ 100 mm/s), we do not observe any significant change in oil encapsulation (see the Appendix for more details), since the pseudostatic assumption holds for the entire velocity range. For the purpose of this work, we keep the u_{av} to be constant with $u_{\mathrm{av}} \approx 3$ mm/s. Based on the above discussion, we assume the interface to be a circular arc in the projected 2D plane such that it satisfies the static contact-angle conditions at the solid boundaries [Fig. 1(c)]. We verify our assumption by fitting the experimental images of the interfaces with a circular arc and observe a reasonably good agreement (see the Appendix for details). A circular interface assumption implies a constant curvature and a constant Laplace pressure drop across the interface. Since the physical process here involves the displacement of oil by water, the relevant contact angle is the advancing contact angle of water in oil $\theta_{a,\mathrm{WO}}$. However, as shown in Fig. 1(c), for simplicity of the calculations, we define θ as the angle subtended by the oil phase with the contact line, i.e., $\theta = \pi - \theta_{a,\mathrm{WO}}$. We assume the center of the post as the

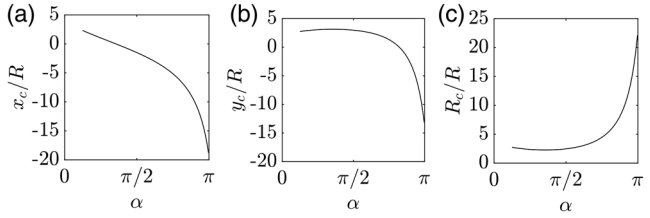

FIG. 2. Variation of (a) x_c/R, (b) y_c/R, and (c) R_c/R with α for $\theta = 37\pi/180$, $\beta = 7\pi/36$, and $W/R = 5$.

origin. The radius of the post is R, the half-width of the channel is W, α is the angle at which the interface touches the post, x_c and y_c are the x and y coordinates of the center of the circular arc, R_c is the radius of the circular arc, and θ and β are the contact angles subtended by oil in water with the contact lines of the post and sidewalls. Through geometrical equations and their simplification, we obtain (see the Appendix for details)

$$y_c = \frac{W\sin(\alpha+\theta) + R\sin\alpha\cos\beta}{\sin(\alpha+\theta)+\cos\beta}, \tag{1}$$

$$x_c = R\cos\alpha + (y_c - R\sin\alpha)/\tan(\alpha+\theta), \tag{2}$$

$$R_c = (W - y_c)/\cos\beta. \tag{3}$$

The above relations define the arc for a general value of α. In Fig. 2, we plot the variation of x_c/R, y_c/R, R_c/R with α for $\theta = 37(\pi/180)$, $\beta = 7\pi/36$, and $W/R = 5$. When the interface meets the posts, i.e., $\alpha = \pi$, the 2D projected interface has very low curvature (or high R_c), as it has only to satisfy the contact-angle condition with sidewalls and is not confined to flow through a smaller area. The curvature sharply increases as the interface moves over the obstacle until $\alpha \approx \pi/2$, where the flow area is minimum. As the interface continues to move (x_c increases with decrease in α), there is a relatively gradual change in y_c and R_c for $\alpha > \pi/2$, since the interface is forced to satisfy the wetting conditions with the two solid surfaces until pinch-off [see Fig. 3(a)].

For a fixed value of α (a time instant in a real experiment), the pressure discontinuity is uniform across the interface and is given by the Laplace pressure, Π_L. We can estimate $\Pi_L \approx \sigma[(1/R_c) + (1/H)]$. Moreover, upon comparing the pressure variation in individual phases over a length equal to the half-width of the channel $\Delta P \sim (12\mu_w u_{\rm av} W/H^2)$ to Laplace pressure Π_L, we get $(\Delta P/\Pi_L) \sim {\rm Ca}(W/H) \sim O(10^{-3})$. Therefore, a pseudostatic assumption, i.e., the pressure variation within each phase is negligible when compared to pressure drop across the interface, is valid. As the interface moves over the post, the interfaces from the two sides of the post eventually touch each other (defined to be $\alpha = \alpha_p$) when $y_c = R_c$ [Fig. 1(c)], leading to a pinch-off and subsequent encapsulation of oil. During pinch-off, we sometimes also observe formation of satellite drops [28] (see the Appendix

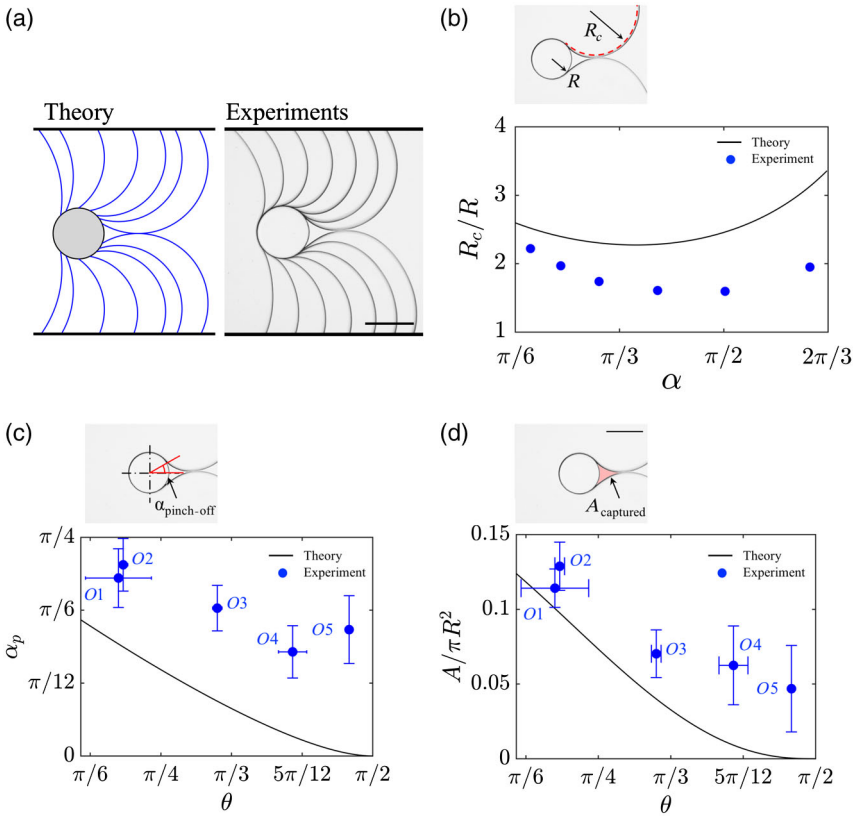

FIG. 3. (a) Comparison of theory and experiment of the oil/water interface evolution for a representative post to verify the hypothesis that the water/oil interface forms a circular arc at low-capillary-number regime. (b) Evolution of R_c with α and the comparison between theory and experiments. (c) Pinch-off position (α_p) vs wettability of the circular obstacle (θ = water-oil-solid contact angle) from theory and experiments. (d) Amount of captured oil vs wettability of the circular obstacle. The amount of captured oil is quantified from the projected area of oil right before pinching off and normalized by the projected area of circular obstacle for each case. $O1$ to $O5$ represent different oil-wet posts having different wetting preferences ($\theta_{O1} = 36°$, $\theta_{O2} = 37°$, $\theta_{O3} = 57°$, $\theta_{O4} = 73°$, and $\theta_{O5} = 85°$ estimated by $\theta = \pi - \theta_{a,\rm WO}$, where $\theta_{a,\rm WO}$ is the experimentally measured advancing contact angle of water in oil). Scale bars are 200 μm.

for details). However, we currently ignore such secondary effects in our model. Using the condition of $y_c = R_c$, we obtain the following relation for α_p upon simplification of Eqs. (A4)–(A6):

$$\frac{R}{W}(1+\cos\beta)\sin\alpha_p + \sin(\alpha_p+\theta) = 1. \quad (4)$$

Equation (4) can be solved analytically to give the following expression for α_p:

$$\alpha_p = 2\tan^{-1}\left(\frac{a' - \sqrt{a'^2+b'^2-1}}{b'+1}\right), \quad (5)$$

where $a' = R/W(1+\cos\beta)+\cos\theta$ and $b' = \sin\theta$.

Let us analyze Eq. (4) in a limiting case of a very wide channel. For $R/W \approx 0$, we obtain $\sin(\alpha+\theta) = 1$ or $\alpha_p = \pi/2 - \theta$. This is an intuitive relation that shows for a more oil-wet post (lower θ), α_p will be higher. In other words, a more oil-wet post can entrap a larger amount of oil. This relation also shows that for neutral ($\theta = \pi/2$) and water-wet posts ($\theta > \pi/2$), $\alpha_p = 0$ and $\alpha_p < 0$, respectively, there will be no oil left on the post [27]. Thus, the model is able to capture key features of the entrapment process.

To calculate the projected area of the trapped liquid pocket, we can solve for the following expression:

$$A = 2\left(\int_{R\cos\alpha_p}^{x_c} f(x)dx - \int_{R\cos\alpha_p}^{R} g(x)dx\right), \quad (6)$$

where $f(x) = y_c - \sqrt{R_c^2-(x-x_c)^2}$ and $g(x) = \sqrt{R^2-x^2}$. An analytical solution can be obtained for Eq. (A9) as follows:

$$A = 2R_c^2\cos(\alpha_p+\theta) - R_c^2\sin(\alpha_p+\theta)\cos(\alpha_p+\theta) - R_c^2\left(\frac{\pi}{2} - (\alpha_p+\theta)\right) - R^2\alpha_p + R^2\cos\alpha_p\sin\alpha_p. \quad (7)$$

We now compare the experimental results and theoretical predictions for posts over a wide range of obstacle contact angles (θ). For theoretical predictions, since we are investigating the advancement of the water interface over a surface, we use $\theta = \pi - \theta_{a,\mathrm{WO}}$ (since θ is defined as the angle subtended by oil with the contact line), where the values of $\theta_{a,\mathrm{WO}}$ are measured experimentally. Also, we use $\beta = 7\pi/36$, which is estimated from the image analysis of the interface in contact with the sidewalls (see the Appendix for more details). Figure 3(a) shows the comparison of theory and experiment of the interface evolution for a representative post. The predicted evolution of the interfacial curvature (R_c) [Eq. (A6)] and the experimental results obtained by fitting images of the interface with a circle given in Fig. 3(b) show similar trends in R_c with α where R_c has a local minimum around $\alpha = \pi/2$, i.e., when the gap between the post and the wall is smallest. In addition, the microscopy images from experiments allow us to calculate the angular position of the interface on the post when pinch-off occurs α_p, and the projected area of the trapped oil A [Figs. 3(c) and 3(d)]. The change of α_p and A with respect to θ shows that for a higher value of θ (less oil wet), lower values of α_p and A are obtained. This is consistent with our expectations, since as the post becomes less oleophilic, the water/oil interfaces from the two sides touch farther downstream, leaving a smaller amount of entrapped oil. While our model correctly predicts trends in the experimental data, we underpredict the values of both α_p and A [Figs. 3(c) and 3(d)]. We attribute the disagreement to (1) the effect of the top and bottom walls currently ignored in our 2D model, (2) deposition of a thin film of oil on the post that might alter the wetting properties, (3) the difference between measuring the contact angles on flat surfaces and the actual contact angles in small microchannels [29], and (4) change in wetting behavior due to surface roughness and contact-angle hysteresis [30,31] (details of contact-angle hysteresis measurements are provided in the Appendix).

B. Two circular posts: Theory and experiments

We investigate the case of two circular posts separated by a center-to-center distance d [Fig. 4(a)]. There are two possibilities that arise in such a case: (1) for $d < d_{\mathrm{crit}}$, the formation of a liquid bridge connecting two posts [Figs. 4(c)(i) and 4(c)(ii)] and (2) for $d \geq d_{\mathrm{crit}}$, the formation of two independent oil pockets [Figs. 4(c)(iii) and 4(c)(iv)]. This liquid bridge formation is particularly interesting since the liquid bridge has a concave shape unlike a typical isolated droplet. Building on the analysis of the single-post case, we develop a theory for two posts to predict the condition for bridging [Fig. 4(a)]. We can augment Eqs. (A4)–(A6) with the following relations from geometric calculations for a bridging system:

$$d = R\cos\alpha + R_c\cos(\alpha+\theta) + (R_c+R)\cos\gamma, \quad (8)$$

$$y_c = (R_c+R)\sin\gamma. \quad (9)$$

For a given d, θ, R, W, β, we can solve for x_c, y_c, R_c, α, and γ by numerically solving Eqs. (A4)–(A6), (A8), and (A9). Therefore, for a given spacing between two circular posts, we can predict whether the liquid bridge will form. Further, for a known θ, R, W, β, $\alpha = \alpha_p$ [Eq. (A8)], we can also solve for $x_c, y_c, R_c, \gamma, d_{\mathrm{crit}}$. Thus, we can also predict the critical distance (d_{crit}) below which a liquid bridge connecting the two posts will form.

For the wetting conditions used in the experiment ($\theta_{O2} = 37°$), we theoretically predict a critical distance of $d_{\mathrm{crit}} \approx 4.9R$, in good agreement with experimental

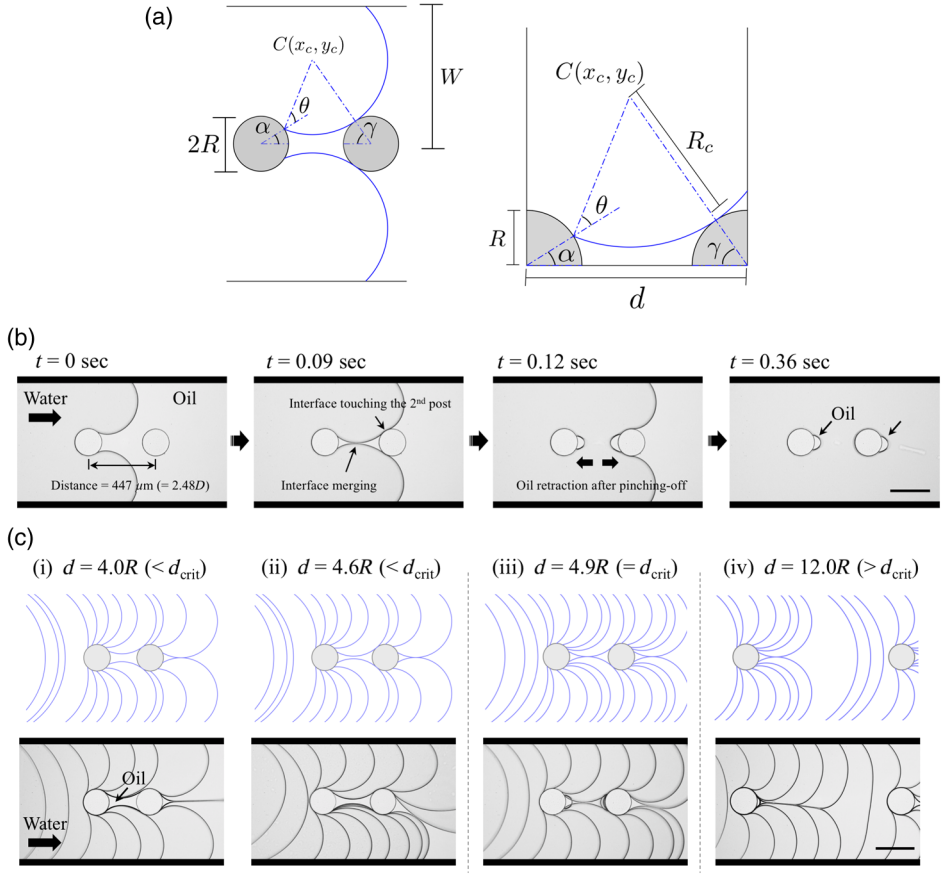

FIG. 4. The two-circular-post case. (a) Theoretical setup for the two-circular-post case. From the geometrical relationship, we can predict a critical interpost distance d_{crit}. (b) Sequential oil-water displacement images for two circular posts when two posts are placed with the critical distance d_{crit}. Water/oil interface meets the first post, and the interface starts to curve around the post. For the critical distance case ($d = d_{crit}$), the water/oil interface simultaneously touches the center line of the channel and the second post. The liquid bridge connecting the two posts is disconnected when the top and bottom interfaces merge together, and the water/oil interface creates the second oil pocket on the second post as the interface moves in the downstream direction. (c) For a given condition, when the interpost distance is closer than the critical distance ($d < d_{crit}$), the oil bridge is formed and connecting the two posts, while when the interpost distance is farther than the critical distance ($d > d_{crit}$), two separate oil pockets are formed. Scale bars are 200 μm.

results. We build four sets of two circular posts in microchannels having four different center-to-center distances [Fig. 4(c)]. Liquid bridges are formed for $d < 4.9R$ [Figs. 4(c)(i) and 4(c)(ii)], and two oil pockets are left for $d \geq 4.9R$ [Fig. 4(c)(iv)]. For the critical case of $d \approx 4.9R$ [Fig. 4(c)(iii)], we observe experimentally that the interfaces meet the center line and touch the second post almost at the same instant [Fig. 4(b), $t = 0.09$ s], and there is formation of an oil pocket on both sides of the second post [Fig. 4(b), $t = 0.12$ s]. The oil pocket that forms at the upstream region of the second post ultimately moves with the advancing interface and is located at the posterior area [Fig. 4(b), $t = 0.36$ s]. With the two-post case, we show that our method allows entrapment of oil in different morphologies (i.e., concave shapes) that is not possible in typical techniques. Moreover, the liquid bridges formed in our system are stable against flow instabilities due to geometric confinement where $R/H > 1$ [32–34].

C. Different shapes and multiple posts

Another way to control liquid entrapment is to exploit the shape of the obstacle. Based on the equation of an obstacle perimeter in the x-y plane, we can define the gradient dy/dx. We propose that if the liquid-liquid interface encounters a sudden change in gradient when moving along the obstacle (i.e., the contact line), the interface attempts to readjust such that it can satisfy the new contact-angle condition. However, during the process of readjustment, the interfaces from the two sides of the obstacle can touch and pinch-off can occur. Hence, we can effectively use the change in slope to suppress the effect of wetting and trap more oil. Here, we choose three additional shapes of posts: square, half-moon, and raindrop. A qualitative comparison of predicted and experimental behavior is provided in Fig. 5(a). We also have good agreement between theory and experiment for the amount of oil trapped with different shapes [Fig. 5(b)]. The evolution of the interface as predicted by theory shows that unlike with a circular shape, the interface "pins" at the point of sudden gradient change of square and half-moon shape and entraps a large amount of oil. We provide detailed derivation of these results in the Appendix. When the interface reaches the corner of the square and half-moon obstacle, two scenarios are possible: (1) during readjustment, the interface touches the center line and pinches off and (2) the interface readjusts to a contact angle of θ with the post, moves inwards, and then pinches off. We show that for a half-moon shape, scenario (1) is valid even for a neutral wet post. In other words, a neutral wet post effectively traps the same amount of oil as that of an oleophilic post. For a square shape, since the change in gradient is lower

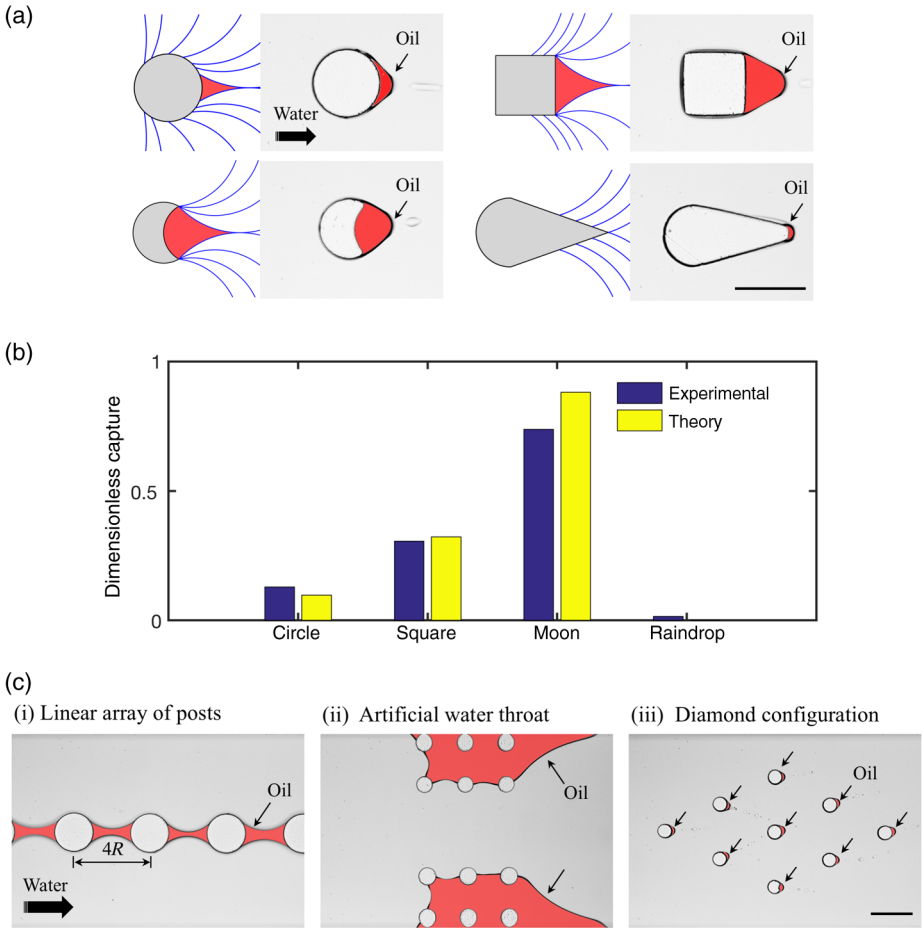

FIG. 5. (a) Predicted interface evolution by theory and experimental result of oil entrapment with different shapes: circle, square, half-moon, and raindrop shapes. (b) Comparison of the normalized amount of capture between theory and experimental data with different obstacle shapes. Projected area of oil is normalized by the area of the posts. (c) Demonstration of the different configurations of multiple post cases. (i) Linear array. Linear array of posts (equally distanced with $4R$) are connected with an oil bridge. (ii) Artificial throat. Six posts near both sides of the walls create an artificial throat by isolating oil pockets on both sides from which water flow is passively guided by the oil pockets. (iii) Diamond configuration. Circular posts distanced farther than their critical distance independently capture oil pockets on each of them. Images are taken in monochrome and processed to highlight the interested area of oil with red color. Scale bars are 200 μm.

compared to the half-moon shape, scenario (1) is valid for a limited range of wetting conditions. We can also design shapes with no gradient change that will effectively trap no oil. For instance, due to the constant gradient along the sides of the raindrop obstacle, the interface "slides" smoothly on the post, and an insignificant amount of oil is left behind at the end. In the Appendix, we show that the contact angle θ has to be less than the half-angle of the triangle to get oil entrapment. Hence, the geometry of the obstacle is another useful design parameter to control the shape and amount of oil entrapment.

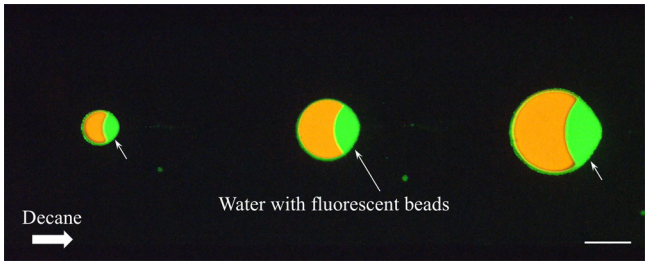

FIG. 6. Water-encapsulation experiment where water and decane are sequentially injected over water-wet posts. For fluorescent imaging, 4% v/v of 0.1 mg/mL rhodamine acrylate (orange) dissolved in poly(ethylene) glycol is added to the prepolymer solution, and 100-nm fluorescent polystyrene microspheres (green) are added in water (10% v/v) in the water/oil displacement. Scale bar is 200 μm.

Based on our understanding of oil entrapment developed with circular and other shaped posts, we can envisage several ways to trap different morphologies of oil pockets [Fig. 5(c)]: (1) a series of posts traps concave-shaped oil pockets by using $d < d_{\mathrm{crit}}$, (2) a throat created by placing multiple posts near the sidewalls to force the interface to stay away from the wall, and (3) compartmentalized oil entrapment to allow for parallel experimentation using a diamond configuration.

As we mention previously, our method also allows us to trap water pockets which we image fluorescently in three different sized polymerized half-moon shapes [Fig. 6]. Further, because we use half-moon-shaped obstacles, we reliably trap a significant amount water behind the post, a feature particularly useful for potential studies in diagnostics and drug discovery.

III. CONCLUSION

In this article, we present a method to trap oil and water pockets in a single step by sequential injection of oil and water (or vice versa) over photopatterned obstacles with

controlled wetting properties. We demonstrate that we can control the amount of trapped liquid by tuning the contact angle as well as the shape of the obstacle. By exploiting the property of wetting, we show the ability to generate concave-shaped pockets and isolated pockets for parallel experimentation. Our platform can be used to create isolated aqueous pockets containing biological entities that can be further probed through subsequent reactions [4], which can be useful in applications such as drug discovery and diagnostics where parallel experimentation is required. The approach can be easily coupled with existing methods to create isolated alginate-based hydrogels [35]. Also, by entrapping controlled amounts of oil, our technique can be used for the screening of chemicals for enhanced oil recovery (EOR). Our work highlights the role of obstacle shape in affecting the amount of oil trapped in a reservoir, an effect that is usually ignored since researchers generally use arrays of cylinders to mimic porous media in microfluidic devices [17,20,22,23,25,36]. As demonstrated in our previous work [27], we can also use this platform to create multiple-liquid compartments by designing structures with heterogeneous wetting (see the Appendix for an example). We hope this work will motivate two phase flow studies in porous media in which shape effects of obstacles are considered. Further, unlike traditional oil-recovery techniques such as core flooding, our platform is compatible with advanced microscopy techniques to provide useful insights into the mechanism of oil release during EOR. Our work can also have implications in fiber coating where one can envision an obstacle as representing the cross section of a fiber. Prior work on fiber wetting or coating is limited to circular cross sections [37,38]. Similarly, the understanding of noncircular shapes can be applied to the coating of nonspherical magnetic particles that are typically synthesized using microfluidic techniques [39,40]. Finally, since our method can be modeled through geometric calculations, it can be a good model system for fundamental studies of multiphase flows and wetting.

ACKNOWLEDGMENTS

We thank Eni SPA for providing funds for this research. H. L. and A. G. contributed equally to this work.

APPENDIX: SUPPLEMENTAL INFORMATION FOR THEORETICAL MODEL AND EXPERIMENTS

1. Theoretical setup of the single circular post

We propose that in the limit of low capillary numbers, the water/oil interface assumes the shape of a circular arc that satisfies contact-angle boundary conditions with solid boundaries [Fig. 7(a)]. We assume the center of the post as the origin, the radius of the post is R, the half-width of the channel is W, α is the angular position of the interface on the post, x_c and y_c are the x and y coordinates of the center of the circular arc, R_c is the radius of the circular arc, and θ and β are the contact angles subtended by oil in water with contact lines of the post and sidewalls.

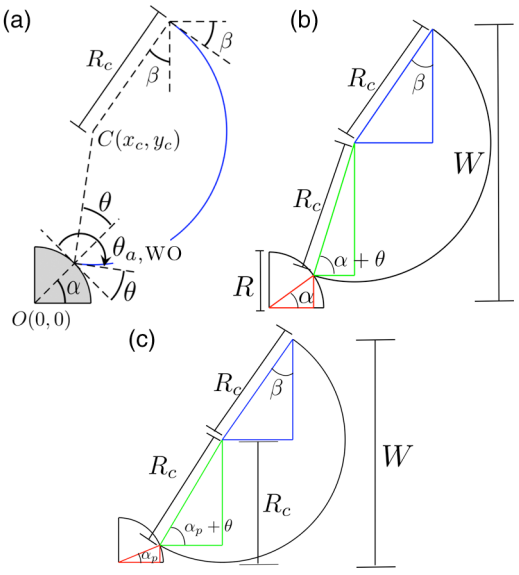

FIG. 7. Theoretical setup for a single circular post. Only the downstream upper half of the post is shown here. (a) Various important angles and lengths in the setup. (b) The geometry is divided into three right-angle triangles to obtain an expression for x_c, y_c, and R_c. (c) Pinch-off condition when $y_c = R_c$.

Here we derive the interface equation, i.e., solve for x_c, y_c, and R_c as a function of R, W, θ, β. We divide the geometry into three right-angle triangles, as shown in the Fig. 7(b). Since at the point of contact between the interface and post, the angle between normal to the post and normal of the interface is θ (as the angle between their tangents is θ), the interface normal makes an angle of $\alpha+\theta$ with the horizontal line. Through geometrical equations, we obtain

$$R\sin\alpha + R_c\sin(\alpha+\theta) + R_c\cos\beta = W, \tag{A1}$$

$$R\sin\alpha + R_c\sin(\alpha+\theta) = y_c, \tag{A2}$$

$$R\cos\alpha + R_c\cos(\alpha+\theta) = x_c. \tag{A3}$$

Solving for y_c, x_c, and R_c, we get

$$y_c = \frac{W\sin(\alpha+\theta) + R\sin\alpha\cos\beta}{\sin(\alpha+\theta)+\cos\beta}, \tag{A4}$$

$$x_c = R\cos\alpha + (y_c - R\sin\alpha)/\tan(\alpha+\theta), \tag{A5}$$

$$R_c = (W - y_c)/\cos\beta. \tag{A6}$$

We can find the condition of pinch-off by noticing that in such a scenario, the interface will touch the central plane, or mathematically, $y_c = R_c$ [Fig. 1(c)]. Using this condition in Eq. (A6), we get

$$R_c = \frac{W}{1+\cos\beta}. \tag{A7}$$

Now using Eq. (A7) in (A1), we get the angular position of pinch-off α_p, the expression for which comes out to be as follows (see Sec. II A):

$$\alpha_p = 2\tan^{-1}\left(\frac{a' - \sqrt{a'^2 + b'^2 - 1}}{b'+1}\right), \tag{A8}$$

where $a' = R/W(1+\cos\beta) + \cos\theta$ and $b' = \sin\theta$. To calculate the projected area of the trapped liquid pocket, we can solve for the following expression:

$$A = 2\left(\int_{R\cos\alpha_p}^{x_c} f(x)dx - \int_{R\cos\alpha_p}^{R} g(x)dx\right), \tag{A9}$$

where $f(x) = y_c - \sqrt{R_c^2 - (x-x_c)^2}$ and $g(x) = \sqrt{R^2 - x^2}$. An analytical solution can be obtained for Eq. (A9) as follows:

$$A = 2R_c^2\cos(\alpha_p+\theta) - R_c^2\sin(\alpha_p+\theta)\cos(\alpha_p+\theta) - R_c^2\left(\frac{\pi}{2} - (\alpha_p+\theta)\right) - R^2\alpha_p + R^2\cos\alpha_p\sin\alpha_p. \tag{A10}$$

The dependence of A with θ is discussed in Sec. II A of the main text.

2. Analysis of obstacles with different shapes

a. Square

We present an analysis to predict the pinch-off condition and amount of trapped liquid for a square obstacle. The upper half of a square obstacle is shown in Fig. 8. We assume the origin to be the center of the square and the half side of the square to be a. When the interface reaches the corner of the square obstacle, the interface encounters a sudden change in gradient and, thus, attempts to readjust to the new contact-angle conditions. There are two scenarios possible in this case: (1) During readjustment, the interface touches the center line and pinches off. In this scenario, the oil-in-water contact angle between the interface and vertical side is θ' such that $\theta' \geq \theta$ [Fig. 8]. (2) The interface readjusts to a contact angle of θ with the vertical side, moves downwards, and pinches off. Here, we discuss only case (1).

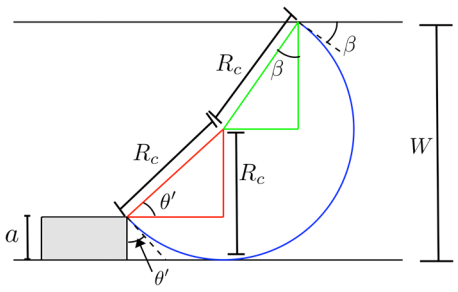

FIG. 8. Theoretical setup for a single square post. θ' is the apparent contact angle at which the pinch-off occurs.

We can write the following equations:

$$R_c + R_c\cos\beta = W, \tag{A11}$$

$$R_c\sin\theta' + a = R_c. \tag{A12}$$

Combining Eqs. (A11) and (A12), we get

$$\theta' = \sin^{-1}\left(1 - \frac{a}{R_c}\right), \tag{A13}$$

$$x_c = a + R_c\cos\theta', \tag{A14}$$

$$y_c = a + R_c\sin\theta', \tag{A15}$$

where $R_c = W/1+\cos\beta$. Using $a = 100\ \mu$m, $\beta = 7\pi/36$, and $W = 500\ \mu$m, we obtain the value of $\theta' = 39.5°$. This is greater than $\theta = 37°$ used in experiments, and, thus, we are in scenario (1). We can calculate the entrapped amount as follows:

$$A = 2\int_a^{x_c}(R_c - \sqrt{R_c^2 - (x-x_c)^2})dx. \tag{A16}$$

Upon integration, we get

$$A = 2\left(R_c^2\cos\theta' - \frac{R_c^2}{2}\cos\theta'\sin\theta' - \frac{R_c^2}{2}\left(\frac{\pi}{2} - \theta'\right)\right). \tag{A17}$$

b. Moon

We present an analysis to predict the pinch-off condition and amount of trapped liquid for a moon-shaped obstacle. The upper half of a moon obstacle is shown in Fig. 9. The moon-shaped geometry is generated by clipping out the overlapping region between two circles from a primary circle. We assume the origin to be the center of the primary circle (from which the overlapping area is subtracted) and the radius of both the circles to be R. The equation of the primary circle is $x^2 + y^2 = R^2$, and the equation of the secondary circle is $(x-R)^2 + y^2 = R^2$. The intersection of the two circles occurs at $x = R/2$, $y = \pm\sqrt{3}R/2$. Thus, we generate the following equations for the moon-shaped obstacle:

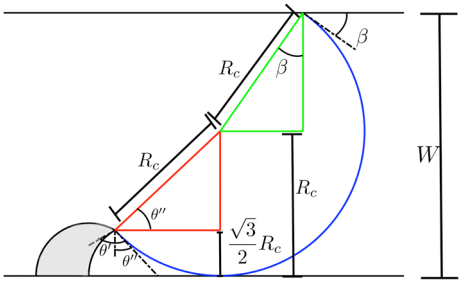

FIG. 9. Theoretical setup for a moon-shaped post. θ' is the apparent contact angle at which the pinch-off occurs.

$$x = R\cos t_1, \qquad y = R\sin t_1, \qquad t_1 = \left[\frac{\pi}{3}, \frac{5\pi}{3}\right], \quad \text{(A18)}$$

$$x = R + R\cos t_2, \qquad y = R\sin t_2, \qquad t_2 = \left[\frac{2\pi}{3}, \frac{4\pi}{3}\right]. \quad \text{(A19)}$$

As the interface moves over the obstacle at $x = R/2$, $y = \pm\sqrt{3}R/2$, the interface attempts to readjust to the new contact-angle conditions. During the process of readjustment, the interfaces meet and pinch-off occurs. Let us assume the apparent contact angle when the pinch-off occurs is θ'. For simplicity, we define $\theta'' = \theta' - \pi/3$, the angle subtended with the vertical by the tangent to the interface. We can derive the following equations:

$$R_c + R_c\cos\beta = W, \quad \text{(A20)}$$

$$R_c\sin\theta'' + \frac{\sqrt{3}}{2}R = R_c. \quad \text{(A21)}$$

Rearranging Eqs. (A20) and (A21), we get

$$\sin\theta'' = \left(1 - \frac{\sqrt{3}R}{2R_c}\right), \quad \text{(A22)}$$

where $R_c = W/1 + \cos\beta$. By using $R = 100\ \mu$m, $W = 500\ \mu$m, $\beta = 7\pi/12$, we get $\theta' = 106.7°$. This shows that a moon-shaped post with even neutral wetting can enable encapsulation since pinch-off will occur as long as $\theta' > \theta$. We can obtain the following result for the area:

$$A = 2R_c^2\cos\theta'' - R_c^2\sin\theta''\cos\theta'' - R_c^2\left(\frac{\pi}{2} - \theta''\right) + \frac{\pi}{3}R^2 - \frac{\sqrt{3}}{4}R^2. \quad \text{(A23)}$$

c. Raindrop

We now discuss the analysis of liquid entrapment behind an obstacle of raindrop shape. The upper half of the obstacle is shown in Fig. 10. The raindrop shape is

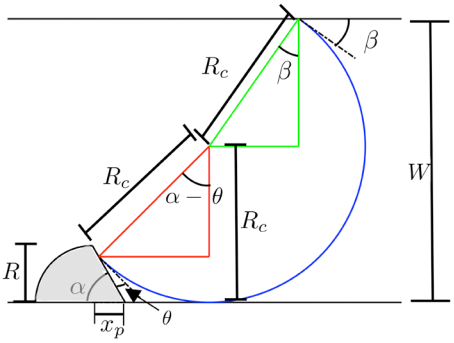

FIG. 10. Theoretical setup for a single-raindrop post with radius R and half-angle α.x_p is the horizontal distance from the vertex of the post from where the interface pinches off.

generated by combining a semicircle with radius R and an isosceles triangle with the diameter of the semicircle as a base, and angle 2α. Therefore, in the upper half, we see a right-angle triangle with side R and angle α. We assume the horizontal distance of the point from where the interface pinches off to the vertex of triangle is x_p [Fig. 10]. Also, if the tangent to the interface at the point of contact makes an angle of θ with the side of the triangle, it can be shown that the normal to the interface makes an angle of $\alpha - \theta$ with the vertical line. This result also leads to an important criterion that the raindrop will only trap liquid when $\alpha \geq \theta$. For the case where we expect to see entrapment, we can write the following equations:

$$R_c + R_c\cos\beta = W, \quad \text{(A24)}$$

$$x_p\tan\alpha + R_c\cos(\alpha - \theta) = R_c. \quad \text{(A25)}$$

Equations (A24) and (A25) can be combined as follows:

$$x_p = R_c\left(\frac{1 - \cos(\alpha - \theta)}{\tan\alpha}\right), \quad \text{(A26)}$$

where $R_c = W/1 + \cos\beta$. For the conditions used in the experiments, $\alpha = 19°$ and $\theta = 37°$, and, thus, we do not expect to see any entrapment. However, for $\alpha \geq \theta$, we can write the following expression for the entrapped area:

$$A = 2R_c^2\sin(\alpha - \theta) - R_c^2\sin(\alpha - \theta)\cos(\alpha - \theta) - R_c^2(\alpha - \theta) - x_p^2\tan\alpha. \quad \text{(A27)}$$

3. Photopolymer composition and contact-angle measurement procedure

Polymeric substrates are prepared with precursor solutions of tabulated concentrations cured under the UV lamp (wavelength 365 nm) for 3 min and thoroughly rinsed with acetone to remove any uncured precursor [Fig. 11(b)].

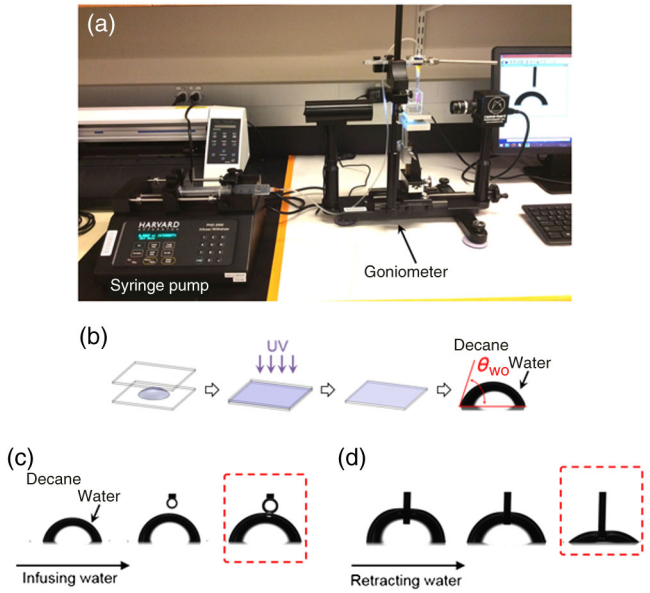

FIG. 11. (a) Contact-angle measurement setup with a syringe pump and a goniometer. (b) Substrates are prepared by pressing a drop of the precursor solution on acrylated glasses. (c) Advancing contact angles are measured when the droplet shows a constant contact angle while the volume and the diameter of the droplet increases. (d) Receding contact angles are measured when the movement of the contact line is detected. The infusing and retracting rates are 5 ml/h, and the maximum volume of the droplet is 20 μl.

A quartz container filled with decane (Sigma-Aldrich) is located on the measurement stage of the contact-angle goniometer (ramé-hart). The prepared substrate is immersed in the decane-filled quartz container, and the needle is set above the substrate surface. Water is infused and withdrawn at a constant injecting or retracting rate (5 ml/h) by a syringe pump (Harvard Apparatus), and the maximum volume of the droplet is 20 μl. The advancing and receding contact angles are measured with an image software (DROPimage Advanced, ramé-hart) when there is an evident contact line change, advanced or retreated, approximately 1 min after the infusion or withdrawal of water is stopped. All measurements are repeated three times, and the average contact angles and the standard deviations are recorded the Table I. For the water-trapping obstacles, we

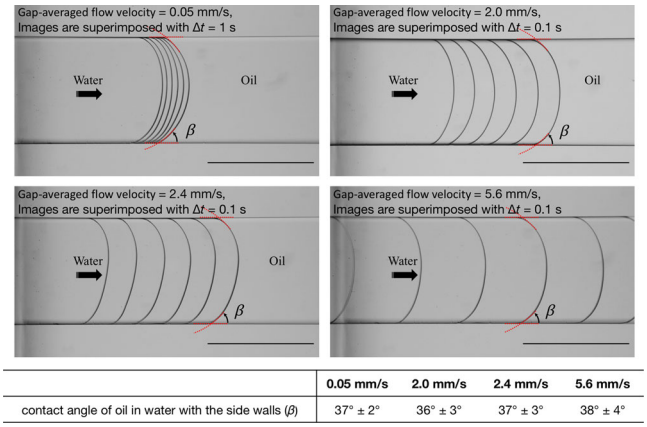

	0.05 mm/s	2.0 mm/s	2.4 mm/s	5.6 mm/s
contact angle of oil in water with the side walls (β)	37° ± 2°	36° ± 3°	37° ± 3°	38° ± 4°

FIG. 12. Sidewall contact angle subtended by the oil phase with the channel sidewalls (β) estimated from time-series microscope images as water displaces oil in an empty microfluidic channel. Scale bar is 1000 μm.

use 60% 2-hydroxyethyl acrylate, 35% 1-(acryloyloxy)-3-(methacryloyloxy)-2-propanol, and 5% 2-hydroxy-2-methylpropiophenon (v/v).

4. Contact angle (β) of oil in water with sidewalls

To define the contact angle (β) with sidewalls for our theoretical model, we prepare an empty microchannel filled with the oil phase. Water is injected using a syringe pump. and time-series microscope images are taken to calculate the contact angle with channel sidewalls [Fig. 12]. We conduct this water displacement with oil experiment for four distinct gap-averaged flow velocities, and we observe similar contact angles for these four flow velocities. We take the value of 35° as the angle subtended by the oil phase with the channel sidewalls (β) for our theoretical model. This contact angle can be seen as counterintuitive because our glass channel has a hydrophilic wetting property. However, we believe this acute oil in water contact angle is because of (1) the presence of a thin layer of oil precoating the channel surface [41,42] and (2) a trapezoidal cross section from anisotropic etching of the glass channel [43]. We also perform the reverse-flow case, i.e., water displacement with oil for four different flow conditions, and obtain a consistent value of 95° subtended by the water with the channel sidewalls. The difference between contact

TABLE I. Photopolymer composition and contact-angle measurement.

	O1	*O2*	*O3*	*O4*	*O5*
Chemical composition (v/v%)					
Cross-linker (1,6-hexanediol diacrylate)	15%	35%	55%	75%	95%
Monomer additive (lauryl acrylate)	80%	60%	40%	20%	0%
Photoinitiator (2-hydroxy-2-methylpropiophenon)	5%	5%	5%	5%	5%
Contact angle (water in oil)					
Advancing contact angle θ_{adv}	144° ± 7°	143° ± 1°	123° ± 1°	107° ± 3°	95° ± 0°
Receding contact angle θ_{rec}	111° ± 10°	103° ± 4°	87° ± 1°	78° ± 2°	82° ± 4°

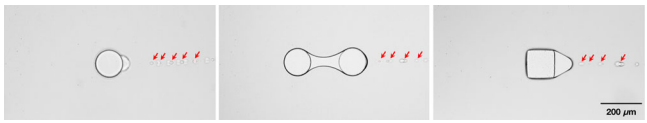

FIG. 13. Example of satellite drop formation during pinch-off for different post geometries.

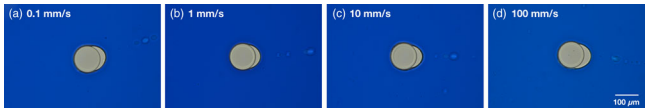

FIG. 14. Oil encapsulation for (a) $u_{av} = 0.1$ mm/s, (b) $u_{av} = 1$ mm/s, (c) $u_{av} = 10$ mm/s, and (d) $u_{av} = 100$ mm/s.

angles depending on the order of displacement corroborates our hypothesis that there is an effect of the precoated phase on the sidewall.

5. Formation of satellite drops during pinch-off

During the process of encapsulation, at pinch-off, we sometimes observe the release of oil through the formation of satellite drops. This phenomenon is observed for different post geometries [Fig. 13]. However, an exact estimation of oil released is beyond the scope of this work.

6. Effect of water flow rate on oil encapsulation

Figure 14 shows the effect of the flow rate on oil encapsulation. We vary the flow rate by 3 orders of magnitude but do not observe any significant change in the amount of oil encapsulated. This is consistent with our expectations since even at $u_{av} = 100$ mm/s, $Ca \ll 1$, and the effect of interfacial tension is dominant.

7. Circular arc approximation for the oil/water interface

We use image analysis to verify the circular arc approximation for the oil/water interface [Fig. 15]. We assume the center of the circular post to be the origin and extract the x, y coordinates of the different oil/water interface (shown as circles). We use only three experimental points to construct circular arcs (shown as solid lines) and observe that the remaining experimental data fall on the constructed arcs, verifying our circular arc approximation. We also show a comparison between experimental data and predicted values by comparing R_c in Fig. 3(b) of the main text.

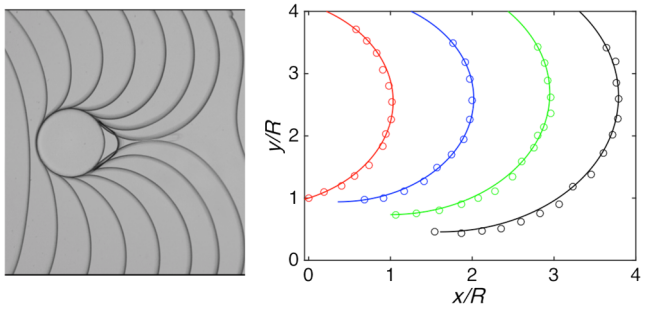

FIG. 15. We extract the x, y coordinates of the oil/water interface using image analysis (shown as circles). We observe that the experimentally extracted data of coordinates fall on the arcs constructed using three data points (shown as solid lines).

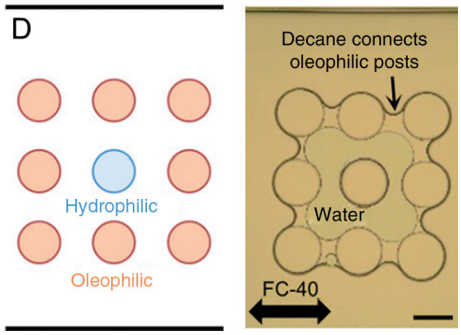

FIG. 16. Demonstration of multiple-liquid compartments using heterogeneous wetting pillars. Three immiscible liquids of water, decane, and fluorinated oil are sequentially injected in a channel with hydrophillic posts surrounded by oleophilic posts. We are able to encapsulate water around the hydrophilic posts and decane around the oleophilic posts. The figure is adapted with permission from Hyundo Lee, Seung Goo Lee, and Patrick S. Doyle, Lab Chip 15, 3047 (2015). Copyright 2015, Royal Society of Chemistry.

8. Encapsulation of multiple-liquid compartments

We can create the multiple-liquid compartment by creating heterogeneous wetting pillars, as demonstrated in our previous work [27]. Figure 16 demonstrates a sequential injection of three different fluids (water, decane, and fluorinated oil) in a channel with a hydrophilic post surrounded by oleophilic posts. Through this approach, we are able to encapsulate both water around the hydrophilic posts and decane around the oleophilic posts.

[1] Jeongyun Kim, David Taylor, Nitin Agrawal, Han Wang, Hyunsoo Kim, Arum Han, Kaushal Rege, and Arul Jayaraman, A programmable microfluidic cell array for combinatorial drug screening, Lab Chip **12**, 1813 (2012).
[2] Amir M. Foudeh, Tohid Fatanat Didar, Teodor Veres, and Maryam Tabrizian, Microfluidic designs and techniques using lab-on-a-chip devices for pathogen detection for point-of-care diagnostics, Lab Chip **12**, 3249 (2012).
[3] Jose L. Garcia-Cordero and Sebastian J. Maerkl, A 1024-sample serum analyzer chip for cancer diagnostics, Lab Chip **14**, 2642 (2014).
[4] Hyewon Lee, Rathi L. Srinivas, Ankur Gupta, and Patrick S. Doyle, Sensitive and multiplexed on-chip microRNA profiling in oil-isolated hydrogel chambers, Angew. Chem. **127**, 2507 (2015).

[5] Burcu Gumuscu, Johan G. Bomer, Albert van den Berg, and Jan C. T. Eijkel, Photopatterning of hydrogel microarrays in closed microchips, Biomacromolecules **16**, 3802 (2015).
[6] Seung Goo Lee, Hyundo Lee, Ankur Gupta, Sehoon Chang, and Patrick S. Doyle, Site-selective *in situ* grown calcium carbonate micromodels with tunable geometry, porosity, and wettability, Adv. Funct. Mater. **26**, 4896 (2016).
[7] Meng Sun, Swastika S. Bithi, and Siva A. Vanapalli, Microfluidic static droplet arrays with tuneable gradients in material composition, Lab Chip **11**, 3949 (2011).
[8] Paul Abbyad, Rémi Dangla, Antigoni Alexandrou, and Charles N. Baroud, Rails and anchors: Guiding and trapping droplet microreactors in two dimensions, Lab Chip **11**, 813 (2011).
[9] Rémi Dangla, Sungyon Lee, and Charles N. Baroud, Trapping Microfluidic Drops in Wells of Surface Energy, Phys. Rev. Lett. **107**, 124501 (2011).
[10] Etienne Fradet, Craig Mcdougall, Paul Abbyad, Rémi Dangla, David Mcgloin, and Charles N. Baroud, Combining rails and anchors with laser forcing for selective manipulation within 2*d* droplet arrays, Lab Chip **11**, 4228 (2011).
[11] Ansgar Huebner, Dan Bratton, Graeme Whyte, Min Yang, Andrew J. deMello, Chris Abell, and Florian Hollfelder, Static microdroplet arrays: A microfluidic device for droplet trapping, incubation and release for enzymatic and cell-based assays, Lab Chip **9**, 692 (2009).
[12] Gabriel Amselem, P. T. Brun, François Gallaire, and Charles N. Baroud, Breaking Anchored Droplets in a Microfluidic Hele-Shaw Cell, Phys. Rev. Applied **3**, 054006 (2015).
[13] Louai Labanieh, Thi N. Nguyen, Weian Zhao, and Dong-Ku Kang, Floating droplet array: An ultrahigh-throughput device for droplet trapping, real-time analysis and recovery, Micromachines **6**, 1469 (2015).
[14] Myeong Chan Jo, Wei Liu, Liang Gu, Weiwei Dang, and Lidong Qin, High-throughput analysis of yeast replicative aging using a microfluidic system, Proc. Natl. Acad. Sci. U.S.A. **112**, 9364 (2015).
[15] Thomas J. Levario, Charles Zhao, Tel Rouse, Stanislav Y. Shvartsman, and Hang Lu, An integrated platform for large-scale data collection and precise perturbation of live drosophila embryos, Sci. Rep. **6**, 21366 (2016).
[16] Myeongwoo Kang, Woohyun Park, Sangcheol Na, Sang-Min Paik, Hyunjae Lee, Jae Woo Park, Ho-Young Kim, and Noo Li Jeon, Capillarity guided patterning of microliquids, Small **11**, 2789 (2015).
[17] Jay W. Grate, Changyong Zhang, Thomas W. Wietsma, Marvin G. Warner, Norman C. Anheier, Bruce E. Bernacki, Galya Orr, and Mart Oostrom, A note on the visualization of wetting film structures and a nonwetting immiscible fluid in a pore network micromodel using a solvatochromic dye, Water Resour. Res. **46**, W11602 (2010).
[18] Marc H. Schneider and Patrick Tabeling, Lab-on-chip methodology in the energy industry: Wettability patterns and their impact on fluid displacement in oil reservoir models, Am. J. Appl. Sci. **8**, 927 (2011).
[19] Naga Siva Kumar Gunda, Bijoyendra Bera, Nikolaos K. Karadimitriou, Sushanta K. Mitra, and S. Majid Hassanizadeh, Reservoir-on-a-chip (ROC): A new paradigm in reservoir engineering, Lab Chip **11**, 3785 (2011).
[20] Kun Ma, Rachel Liontas, Charles A. Conn, George J. Hirasaki, and Sibani Lisa Biswal, Visualization of improved sweep with foam in heterogeneous porous media using microfluidics, Soft Matter **8**, 10669 (2012).
[21] Mengjie Wu, Feng Xiao, Rebecca M. Johnson-Paben, Scott T. Retterer, Xiaolong Yin, and Keith B. Neeves, Single-and two-phase flow in microfluidic porous media analogs based on Voronoi tessellation, Lab Chip **12**, 253 (2012).
[22] Pranab Kumar Mondal, Debabrata Das Gupta, and Suman Chakraborty, Interfacial dynamics of two immiscible fluids in spatially periodic porous media: The role of substrate wettability, Phys. Rev. E **90**, 013003 (2014).
[23] Pierre Horgue, Frédéric Augier, Paul Duru, Marc Prat, and Michel Quintard, Experimental and numerical study of two-phase flows in arrays of cylinders, Chem. Eng. Sci. **102**, 335 (2013).
[24] Sujit S. Datta, Jean-Baptiste Dupin, and David A. Weitz, Fluid breakup during simultaneous two-phase flow through a three-dimensional porous medium, Phys. Fluids **26**, 062004 (2014).
[25] Marta S. de La Lama and Martin Brinkmann, Impact of wettability correlations on multiphase flow through porous media, arXiv:1205.7026.
[26] Ali Q. Raeini, Branko Bijeljic, and Martin J. Blunt, Modelling capillary trapping using finite-volume simulation of two-phase flow directly on micro-CT images, Adv. Water Resour. **83**, 102 (2015).
[27] Hyundo Lee, Seung Goo Lee, and Patrick S. Doyle, Photopatterned oil-reservoir micromodels with tailored wetting properties, Lab Chip **15**, 3047 (2015).
[28] Bala Ambravaneswaran, Hariprasad J. Subramani, Scott D. Phillips, and Osman A. Basaran, Dripping-Jetting Transitions in a Dripping Faucet, Phys. Rev. Lett. **93**, 034501 (2004).
[29] Xingxun Li, Xianfeng Fan, and Stefano Brandani, Difference in pore contact angle and the contact angle measured on a flat surface and in an open space, Chem. Eng. Sci. **117**, 137 (2014).
[30] David Quéré, Wetting and roughness, Annu. Rev. Mater. Res. **38**, 71 (2008).
[31] H. B. Eral, D. J. C. M. 't Mannetje, and J. M. Oh, Contact angle hysteresis: A review of fundamentals and applications, Colloid Polym. Sci. **291**, 247 (2013).
[32] Pierre Guillot, Annie Colin, Andrew S. Utada, and Armand Ajdari, Stability of a Jet in Confined Pressure-Driven Biphasic Flows at Low Reynolds Numbers, Phys. Rev. Lett. **99**, 104502 (2007).
[33] Pierre Guillot, Annie Colin, and Armand Ajdari, Stability of a jet in confined pressure-driven biphasic flows at low Reynolds number in various geometries, Phys. Rev. E **78**, 016307 (2008).
[34] Katherine J. Humphry, Armand Ajdari, Alberto Fernández-Nieves, Howard A. Stone, and David A. Weitz, Suppression of instabilities in multiphase flow by geometric confinement, Phys. Rev. E **79**, 056310 (2009).
[35] Stefanie Utech, Radivoje Prodanovic, Angelo S. Mao, Raluca Ostafe, David J. Mooney, and David A. Weitz, Microfluidic generation of monodisperse, structurally homogeneous alginate microgels for cell encapsulation and 3*d* cell culture, Adv. Healthcare Mater. **4**, 1628 (2015).

[36] Benzhong Zhao, Christopher W. MacMinn, and Ruben Juanes, Wettability control on multiphase flow in patterned microfluidics, Proc. Natl. Acad. Sci. U.S.A. **113**, 10251 (2016).

[37] Alban Sauret, François Boulogne, David Cébron, Emilie Dressaire, and Howard A. Stone, Wetting morphologies on an array of fibers of different radii, Soft Matter **11**, 4034 (2015).

[38] S. Protiere, C. Duprat, and H. A. Stone, Wetting on two parallel fibers: Drop to column transitions, Soft Matter **9**, 271 (2013).

[39] Byeong-Ui Moon, Navid Hakimi, Dae Kun Hwang, and Scott S. H. Tsai, Microfluidic conformal coating of non-spherical magnetic particles, Biomicrofluidics **8**, 052103 (2014).

[40] Scott S. H. Tsai, Jason S. Wexler, Jiandi Wan, and Howard A. Stone, Conformal coating of particles in microchannels by magnetic forcing, Appl. Phys. Lett. **99**, 153509 (2011).

[41] Daniel Bonn, Jens Eggers, Joseph Indekeu, Jacques Meunier, and Etienne Rolley, Wetting and spreading, Rev. Mod. Phys. **81**, 739 (2009).

[42] Hooman Foroughi, Alireza Abbasi, Kausik S. Das, and Masahiro Kawaji, Immiscible displacement of oil by water in a microchannel: Asymmetric flow behavior and nonlinear stability analysis of core-annular flow, Phys. Rev. E **85**, 026309 (2012).

[43] Michiel Musterd, Volkert van Steijn, Chris R. Kleijn, and Michiel T. Kreutzer, Calculating the volume of elongated bubbles and droplets in microchannels from a top view image, RSC Adv. **5**, 16042 (2015).